


Cite this: *RSC Adv.*, 2023, 13, 5874

# CeO<sub>2</sub>@NH<sub>2</sub> functionalized electrodes for the rapid detection of SARS-CoV-2 spike receptor binding domain

Ayu Triastuti,<sup>a</sup> Salma Nur Zakiyyah,<sup>a</sup> Shabarni Gaffar,<sup>ab</sup> Isa Anshori,<sup>bc</sup> Akhmadi Surawijaya,<sup>d</sup> Darmawan Hidayat,<sup>e</sup> Hesti Lina Wiraswati,<sup>f</sup> Muhammad Yusuf<sup>ab</sup> and Yeni Wahyuni Hartati<sup>\*ab</sup>

A detection method based on an electrochemical aptasensor has been developed as an alternative fast, portable, simple, inexpensive, and high-accuracy detection method for detecting the SARS-CoV-2 Spike Receptor Binding Domain (spike RBD). The CeO<sub>2</sub>@NH<sub>2</sub> functionalized Screen Printed Carbon Electrode (SPCE) was used to immobilize an aminated aptamer of spike RBD protein via glutaraldehyde as a linker. The aptamer's interaction with the SARS-CoV-2 Spike RBD was measured via the [Fe(CN)<sub>6</sub>]<sup>4−/3−</sup> redox system signal. Experimental conditions were optimized using a Box–Behnken experimental design and showed that the optimal conditions of the SARS-CoV-2 aptasensor were 1.5 ng mL<sup>−1</sup> of aptamer, immobilization of aptamer for 60 minutes, and Spike RBD incubation for 10 minutes. The developed aptasensor was able to detect the standard SARS-CoV-2 Spike RBD with a detection limit of 0.017 ng mL<sup>−1</sup> in the range of 0.001–100 ng mL<sup>−1</sup>. This aptasensor was used to detect salivary and oropharyngeal swab samples of normal individuals with the addition of Spike RBD, and the recoveries were 92.96% and 96.52%, respectively. The testing on nasopharyngeal swab samples of COVID-19 patients showed that the aptasensor results were comparable with the qRT-PCR results. Thus, the developed aptasensor has the potential to be applied as a SARS-CoV-2 rapid test method for clinical samples.

Received 28th November 2022  
Accepted 9th February 2023

DOI: 10.1039/d2ra07560a

rsc.li/rsc-advances

## 1 Introduction

COVID-19 is typical pneumonia and acute respiratory distress syndrome with a high risk of death caused by Severe Acute Respiratory Syndrome Coronavirus-2 (SARS-CoV-2). The human-to-human transmission of this highly infectious zoonotic virus has grown exponentially with the emergence of millions of cases resulting in a worldwide pandemic. Up to October 2022, there were more than 615 million confirmed cases, with more than 6.5 million deaths.<sup>1</sup> Today, although the number of cases has decreased and some countries have declared the pandemic is over, there are still many confirmed COVID-19 patients. Therefore, a rapid method is needed for the detection of SARS-CoV-2.

The SARS-CoV-2 genome is a single-strand positive-sense RNA (+ssRNA) that encodes non-structural proteins ORF1 and ORF2 as well as several structural proteins, such as spike (S), membrane protein (M), and envelope protein (E). Spike is a large 180 kDa glycoprotein that consists of two domains, the S1-RBD (Receptor Binding Domain) and the S2 (fusion domain). The Spike RBD plays a role in the internalization of the virus by interaction with the receptor of angiotensin-converting enzyme 2 (ACE-2) on the surface of target cells, primarily the extracellular portion of the epithelial cells of the respiratory tract.<sup>2</sup> The Spike RBD plays a role in the formation of an immune response of the host cells, therefore it is widely used as a biomarker for the detection of SARS-CoV-2 in the immunochemistry-based methods.<sup>3–5</sup>

The gold standard method for SARS-CoV-2 detection is real-time reverse transcriptase PCR (rtRT-PCR/qPCR), using a specific probe to detect several target genes.<sup>4,6–8</sup> The main limitations of this method are; time-consuming, requires expensive equipment and reagents, as well as trained laboratory personnel. The second widely utilized technique is an antigen-based diagnostic test employing lateral flow immunoassay (LFIA), which is quicker than qPCR but less sensitive.<sup>9,10</sup>

Several studies have also reported the use of electrochemical biosensors to detect the SARS-CoV-2 virus. Some of them are: the electrochemical immunosensor by using a working

<sup>a</sup>Department of Chemistry, Faculty of Mathematics and Natural Sciences, Universitas Padjadjaran, Indonesia. E-mail: yeni.w.hartati@unpad.ac.id

<sup>b</sup>Molecular Biotechnology and Bioinformatics Research Center, Universitas Padjadjaran, Indonesia. E-mail: isaa@staff.stei.itb.ac.id; isa\_anshori@stei.itb.ac.id

<sup>c</sup>Lab-on-Chip Group, Biomedical Engineering Department, School of Electrical Engineering and Informatics, Bandung Institute of Technology, Indonesia

<sup>d</sup>Center of Excellence on Microelectronics, School of Electrical Engineering and Informatics, Bandung Institute of Technology, Bandung, Indonesia

<sup>e</sup>Department of Electrical Engineering, Faculty of Mathematics and Natural Sciences, Universitas Padjadjaran, Indonesia

<sup>f</sup>Department of Parasitology Faculty of Medicine, Universitas Padjadjaran, Indonesia



electrode functionalized with graphene-anti-spike for detection of the RBD,<sup>11</sup> modification of electrode using cobalt-TiO nanotubes (Co-TNTs) monoclonal antibody as a detection platform for SARS-CoV-2,<sup>1</sup> modified carbon black printed electrode with magnetic beads and antibodies,<sup>12</sup> PET-gold electrode with monoclonal antibody,<sup>13</sup> functionalized gold nanoparticle (AuNP)/nCoV-19Ab,<sup>9</sup> e-Covsens based on SPCE-Ab nCovid-19 with fluorine-doped tin oxide electrode (FTO-AuNPs),<sup>14</sup> and a ProtA/CuONC nano-bio device-SPCE as a substrate to direct the orientation of IgG antibodies, as a specific receptor for the detection of spike glycoproteins.<sup>15</sup> The electrochemical biosensor detection method is rapid, low cost, easy operation, small sample size, and portable, allowing on-the-spot testing, as well as high sensitivity and selectivity for medical sample analysis.<sup>13,15–20</sup>

The use of antibodies as a bioreceptor molecules has several disadvantages because they are large molecules susceptible to high temperatures and changes in pH so they can be easily denatured.<sup>21</sup> The aptamer is a single-strand DNA or RNA oligonucleotide that has a secondary structure that can interact with antigens. It has several advantages that highlight its use as a bioreceptor, such as specific with high affinity, small size (BM 20 kDa), a specific three-dimensional structure that complements the target, stability to extreme temperature and pH changes, and can return to its initial conformation when denatured.<sup>21–23</sup>

An aptasensor is a biosensor that uses an aptamer as a bioreceptor.<sup>24–26</sup> The size of an aptamer is smaller (2–3 nm) than an antibody (12–15 nm), thereby reducing the steric barrier to the surface of the coronavirus, which is about 100 nm. A smaller bioreceptor will enable more molecules to bind to the same surface area. Song *et al.* have reported two aptamers that target SARS-CoV-2 Spike RBD using the ACE2 receptor competition-based selection strategy (SELEX). The published aptamers by Song *et al.* have drawn the interest of researchers working on constructing electrochemical aptasensor.<sup>27–31</sup> An electrochemical aptamer-based sensor created by Idili *et al.* was tested directly on saliva samples. Additionally, Zakashansky *et al.* developed an aptasensor for saliva samples with a detection limit of 1 ng mL<sup>−1</sup>. In this work, a hairpin-structure of 51-base aptamer with a dissociation constant of 5.8 nM was studied. The aptamer binds to several amino acids of RBD, which is important for highly specific detection.<sup>2</sup>

On the other hand, modification of the working electrode surface is important to increase the selectivity and sensitivity of the sensor, as well as the efficient immobilization of biomolecules on the electrode surface.<sup>15,32–34</sup> Cerium oxide has been reported to have beneficial properties, such as being non-toxic, having good electrical conductivity, being inert, large surface area, and being biocompatible.<sup>35–37</sup> In addition, the excellent conductance properties of cerium play an important role in the electron transfer process.<sup>38</sup> Various studies related to electrode modification with cerium oxide have been reported. Cerium oxide can be directly conjugated to the electrode surface or functionalized with other materials.<sup>39</sup> The use of amino silane groups as a coupling agent can activate cerium oxide for functionalization with amine groups.<sup>36,40–43</sup>

Immobilization is a key step in the aptasensor fabrication process because it will affect the overall performance of the electrochemical sensor. An immobilized bioreceptor with good orientation and the stability of the bioreceptor on the electrode surface allows an increase in the binding capacity of the target.<sup>15,44</sup> Glutaraldehyde is a highly reactive dialdehyde compound that functions as a crosslinker in biological tests and coupling aldehyde (–COH) groups at both glutaraldehyde terminals will spontaneously crosslink with the amine (NH) group from the surface of the electrode and the aptamer through a condensation reaction to form an amide bond.<sup>45,46</sup>

In addition, another thing related to testing is the type of sample. Generally, the specimens used for testing for COVID-19 are nasopharyngeal specimens, which are considered uncomfortable to cause bleeding for some patients. Alternative saliva is available as a non-invasive diagnostic fluid. The copy of viral particles in the saliva sample is about 102–1011 copies per ml during the infection period.<sup>28</sup> The oral cavity communicates with the nasopharynx by continuously mixing nasopharyngeal secretions with saliva, leading to a mixed salivary nasopharyngeal environment. In particular, saliva has been used for the detection of the coronaviruses responsible for Severe Acute Respiratory Syndrome (SARS-CoV) and Middle East respiratory syndrome (MERS). Saliva contains a collection of viruses donated from the oral nasopharynx and lower respiratory tract secretions. Also, oral epithelial cells and salivary glands have increased expression of ACE-2 receptors for viruses. The salivary viral load is highest in the first week after clinical manifestations of the disease and can last for more than 3 weeks.<sup>47,48</sup> Interestingly, the sensitivity of salivary tests in the diagnosis of COVID-19 is about 91% (95% CI; 80% to 99%) compared to the nasopharyngeal swab (NPS), which is about 98% (95% CI; 89% to 100%), which is quite good; similar due to the considerable overlap of confidence intervals.<sup>48</sup>

This study is involved in the development of an electrochemical aptasensor for rapid test detection of SARS-CoV-2 Spike RBD in Indonesia. The sensor device consists of the CeO<sub>2</sub>-modified SPCE using 3-aminopropyl-triethoxysilane and glutaraldehyde as linkers and aptamer as a bioreceptor. The electrode is connected to differential pulse voltammetry (DPV) measurements *via* the [Fe(CN)<sub>6</sub>]<sup>4−/3−</sup> redox system responses. The aptasensor performance was assessed using saliva and oropharyngeal swab samples.

## 2 Experimental

### 2.1 Materials

The materials used in this study were 3-aminopropyl triethoxysilane (APTES) (Sigma Aldrich); aptamer DNA sequence was based on Song *et al.* (2020) – [C<sub>6</sub>-NH<sub>2</sub>]-CAG CAC CGA CCT TGT GCT TTG GGA GTG CTG GTC CAA GGG CGT TAA TGG ACA that was synthesized by Bioneer Corporation. Bovine serum albumin (BSA), cerium nitrate hydrate (Ce [NO<sub>3</sub>]<sub>3</sub>·6H<sub>2</sub>O), glutaraldehyde 50%, phosphate buffer saline (PBS) pH 7.4, and solid potassium ferricyanide K<sub>3</sub>[Fe(CN)<sub>6</sub>] (Sigma Aldrich); potassium chloride (KCl) (Merck), sodium hydroxide (NaOH) (Merck, pa); SARS-CoV-2 Spike RBD



(GenScript, USA), double distilled water (PT. Ikapharmindo Putramas Indonesia), and inactivated avian virus (H5N1) was a gift from PT. Tekad Mandiri Citra, Bandung, Indonesia. Clinical samples of COVID-19 patients used in this study were obtained from the Covid-19 test laboratory (C-29 Lab.) at Padjadjaran University.

## 2.2 Electrochemical measurements

All electrochemical measurements were conducted using a Zimmer & Peacock potentiostat connected to a computer using the PS Trace 5.4 software (Zeamer & Peacock, UK). The three-electrode system (GSI Technologies, LLC, USA) consists of an SPCE as a working electrode, an Ag/AgCl pseudo reference electrode, and a carbon auxiliary electrode. The working, reference, and counter electrodes are integrated into the screen-printed carbon electrode. The diameter of the working electrode is 5 mm and its working area is 0.019 cm<sup>2</sup>. The modified electrode was characterized using a scanning electron microscope JSM-7500F (Jeol, US), FTIR spectrophotometer (Spectrum Pekin Elmer 100), and UV-Vis spectrophotometer (Thermo Scientific, USA). The clinical samples study was conducted within the Biological Safety Cabinet Class II in the C-29 Laboratory.

## 2.3 Preparation of cerium oxide (CeO<sub>2</sub>)

CeO<sub>2</sub> was synthesized by the precipitation method. First, 2.0 g of solid Ce(NO<sub>3</sub>)<sub>3</sub> were dissolved in 25 mL double distilled water, then 25 mL of 0.3 M NaOH was added dropwise. The mixture was stirred continuously for 2–3 hours at room temperature until a pale yellowish precipitate formed. The precipitate was separated and washed several times with double distilled water and alcohol, then dried at 70 °C for 2 hours. The yellowish particles obtained were then calcined at 240 °C for 10 hours to form cubic structures of nano ceria.<sup>41,49</sup>

## 2.4 Preparation of cerium oxide functionalized amine (CeO<sub>2</sub>@NH<sub>2</sub>)

Fifty-one microliters of APTES were dissolved in 20 mL ethanol : aqua dm = 1 : 3 and stirred for 30 minutes, then 68 mg of solid CeO<sub>2</sub> was added and stirred for 2 hours at 69.85 °C. The resulting pale-yellow precipitate of CeO<sub>2</sub>@NH<sub>2</sub> was filtered and dried at 109 °C overnight, then weighed and stored at room temperature before use.<sup>40</sup>

## 2.5 Modification of SPCE by (CeO<sub>2</sub>@NH<sub>2</sub>)

The SPCE was rinsed several times using double distilled water, then dropped with 40 µL of CeO<sub>2</sub>@NH<sub>2</sub> and incubated for 24 hours. Then, the electrodes were carefully washed with aqua pro injection and dried at room temperature. The CeO<sub>2</sub>@NH<sub>2</sub> modified SPCE was characterized by scanning electron microscopy (SEM-EDS), DPV, and electrochemical impedance spectroscopy (EIS) using a [Fe(CN)<sub>6</sub>]<sup>4−/3−</sup> redox system.

## 2.6 Fabrication of the aptasensor

SPCE-CeO<sub>2</sub>@NH<sub>2</sub> was dropped with 20 µL of 2.5% glutaraldehyde (GA) and incubated for 1 hour at room temperature, GA will form a covalent bond with CeO<sub>2</sub>@NH<sub>2</sub>. The electrodes were rinsed with double distilled water to remove non-specific species that do not stick to the electrode surface. Then, 20 µL of aptamer was dropped/immobilized on the surface of the electrode and incubated for 60 minutes at room temperature. The electrodes were rinsed with 0.01 M PBS pH 7.4 to remove the unbound aptamer species. The empty surface of the electrodes was blocked using 1% BSA and incubated for 20 minutes at room temperature, and then the electrodes were rinsed with 0.01 M PBS pH 7.4. Finally, the standard Spike RBD was dropped on the electrode surface and incubated for 15 minutes at room temperature. The aptasensor response was measured

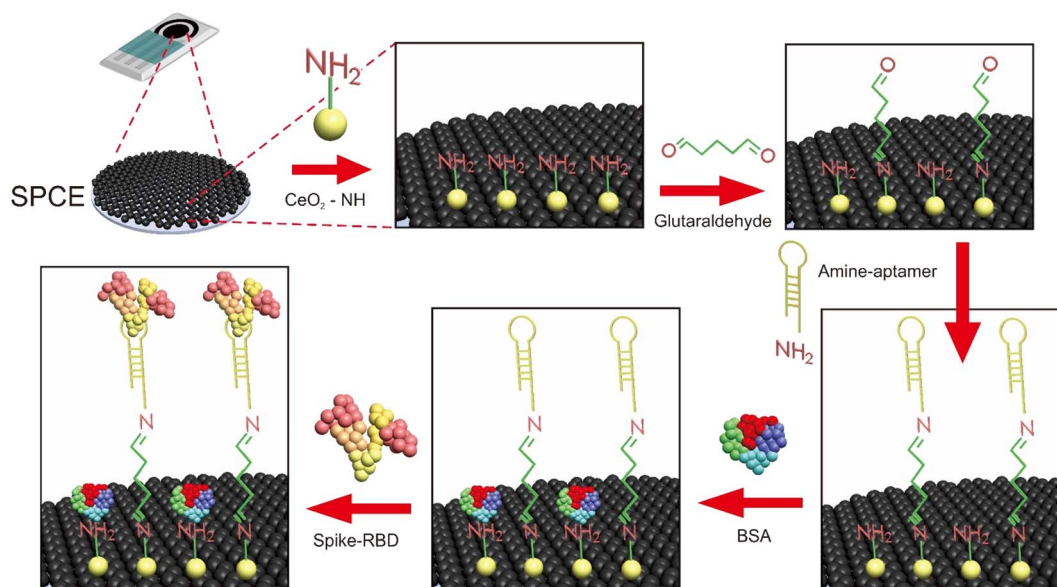


Fig. 1 Schematic of aptasensor platform for detection of Spike RBD SARS-CoV-2.



Table 1 Optimization of experiments conditions using Box–Behnken

Factor	Unit	Level		
		−1	0	+1
Aptamer concentration ( $X_1$ )	$\mu\text{g mL}^{-1}$	0.5	1.0	1.5
Immobilization time ( $X_2$ )	min	30	60	90
Incubation time of target ( $X_3$ )	min	5	10	15

electrochemically by EIS with the frequency 0.1–1 000 000 Hz and DPV with the potential range −1.0 V to +1 V scanning rate of  $0.008 \text{ V s}^{-1}$  using the  $[\text{Fe}(\text{CN})_6]^{4-/3-}$  10 mM redox system in 0.1 M KCl. The schematic of aptasensor is shown in Fig. 1.

### 2.7 Optimization of the experimental conditions using a Box–Behnken experimental design

Three factors were optimized by the Box–Behnken experimental design using the Minitab 18, that were: aptamer concentration ( $X_1$ ), aptamer immobilization time ( $X_2$ ), and Spike RBD incubation time ( $X_3$ ) via three different levels, the lowest level (−1), medium (0), and highest (+1) as shown in Table 1.

### 2.8 Calibration curve, the limit of detection and limit of quantification

The standard Spike RBD (0.001, 0.01, 0.05, 0.1, 1.0, 10, and 100  $\text{ng mL}^{-1}$ ) was tested on the aptasensor using the optimal experimental conditions and the resulting electrochemical response was measured by DPV using a redox system of 10 mM  $[\text{Fe}(\text{CN})_6]^{4-/3-}$  in 0.1 M KCl with a scanning rate of  $0.008 \text{ V s}^{-1}$  and a range of −1.0 V to +1.0 V.

A calibration curve of the concentration *versus* the mean peak current difference ( $\Delta I$ ) for each measurement was plotted to determine the detection limit (LOD), the quantification limit (LOQ), precision, and accuracy. The selectivity of the aptasensor was then evaluated using a negative control, Spike RBD, and inactivated influenza virus (H5N1).

### 2.9 Aptasensor response for salivary and oropharyngeal swab samples

Salivary and oropharyngeal swabs from normal individual were diluted to 5 mL of 0.01 M PBS 7.4. The % recovery was determined by addition of a specific concentration of the standard Spike RBD to the sample. The resulting electrochemical response was measured by DPV.

## 3 Results and discussion

### 3.1 Characterization of $\text{CeO}_2@/\text{NH}_2$ and SPCE- $\text{CeO}_2@/\text{NH}_2$

Fig. 2A shows the absorption of  $\text{CeO}_2$  that synthesized by alkaline precipitation method from the precursor  $\text{Ce}(\text{NO}_3)_3$ . The maximum absorption wavelength of nanoceria is generally at 250–400 nm related to the band gap energy and the charge transition between O (2p) and Ce (4f) expressed in  $\text{O}_2$  and  $\text{Ce}^{4+}$ . Moreover, the maximum absorption peak of nanoceria shifted toward lower wavelengths, which is associated with the

quantum confinement effect due to the decrease in particle size. The band gap energy is incorporated with the transition between valence and conduction band in ceria.<sup>41,49,50</sup>

Fig. 2B shows the SEM images of  $\text{CeO}_2$  powder. The cerium oxide nanoparticles was found to form aggregates, which may have been caused by an inadequately high synthesis temperature that prevented the particles from being evenly dispersed and supported by dynamic light scattering. The particle analyzer's findings showed that the average size distribution was 288.9 nm (Fig. 2C). However, the particle size analyzer data is usually far from the nanomaterial size calculated by the Scherer equation using the X-ray diffraction method.<sup>51</sup>

Fig. 2D shows the FTIR spectra of synthesized  $\text{CeO}_2$  and  $\text{CeO}_2$  functionalized APTES. The wavelength range of  $3434.7 \text{ cm}^{-1}$  and  $3433.1 \text{ cm}^{-1}$  correlates to O–H groups derived from the solvent and the C–H groups of the organic solvent at  $2099 \text{ cm}^{-1}$  and  $2099.1 \text{ cm}^{-1}$ . The stretching vibration at  $1643.9 \text{ cm}^{-1}$  and  $1644.7 \text{ cm}^{-1}$  confirm H–OH and the wavelength of  $615.8 \text{ cm}^{-1}$  correlates to the binding of Ce–O.<sup>50</sup> The peak of Ce–O bond occurs at  $500\text{--}700 \text{ cm}^{-1}$ , presumed to be the binding of silane with cerium, Si–O–Ce. The peaks at  $535.1 \text{ cm}^{-1}$ , which then shift to  $710.9 \text{ cm}^{-1}$ ,  $519.2 \text{ cm}^{-1}$ , and  $511.8 \text{ cm}^{-1}$ ,  $528.0 \text{ cm}^{-1}$ , are suspected to be Ce–O–Si. The weak transmittance of about 59% at  $1459 \text{ cm}^{-1}$  indicates the  $\text{NH}_2$  group.

Bare SPCE and SPCE- $\text{CeO}_2@/\text{NH}_2$  were characterized by SEM-EDS to determine the morphology and verify the presence of  $\text{CeO}_2@/\text{NH}_2$  on the electrode surface. Fig. 3A shows the SPCE component which consists of reference, working, and counter electrodes. The working electrode is the location for depositing  $\text{CeO}_2@/\text{NH}_2$ . Fig. 3B shows the elements C, O, N, Ce, Si, and N derived from the modification of  $\text{CeO}_2@/\text{NH}_2$  to the surface of the carbon electrode. Fig. 3C shows the homogeneous smooth surface of bare SPCE, while the white spots distributed on the surface are  $\text{CeO}_2@/\text{NH}_2$  coated carbon working electrode of SPCE (Fig. 3D).

### 3.2 Evaluation of the aptasensor through electrochemical analyses

In order to study the effect of the  $\text{CeO}_2@/\text{NH}_2$  on the sensitivity, SPCE working electrodes modified with  $\text{CeO}_2@/\text{NH}_2$  were tested electrochemically. Fig. 4 shows the current response of  $[\text{Fe}(\text{CN})_6]^{4-/3-}$  electrodes without and with  $\text{CeO}_2@/\text{NH}_2$  modification. This result indicates that the current response of the electrode containing  $\text{CeO}_2@/\text{NH}_2$  increases dramatically.

Each process in the modification of SPCE by  $\text{CeO}_2@/\text{NH}_2$  was characterized by Differential Pulse Voltammetry (DPV). Fig. 4A shows the DPV response of  $[\text{Fe}(\text{CN})_6]^{4-/3-}$  on the SPCE- $\text{CeO}_2@/\text{NH}_2$ -GA, SPCE- $\text{CeO}_2@/\text{NH}_2$ -Aptamer, and SPCE- $\text{CeO}_2@/\text{NH}_2$ -Aptamer-Spike RBD. Peak current measurements showed that  $\text{CeO}_2@/\text{NH}_2$  had been conjugated to the electrode surface, measuring  $5.072 \mu\text{A}$  at the SPCE's bare (curve a) and  $17.877 \mu\text{A}$  at SPCE- $\text{CeO}_2@/\text{NH}_2$  (curve b). These results confirm that  $\text{CeO}_2@/\text{NH}_2$  is already conjugated to the electrode surface, and SPCE- $\text{CeO}_2@/\text{NH}_2$  is more conductive than bare SPCE. The increase in current at low potential can be attributed to the





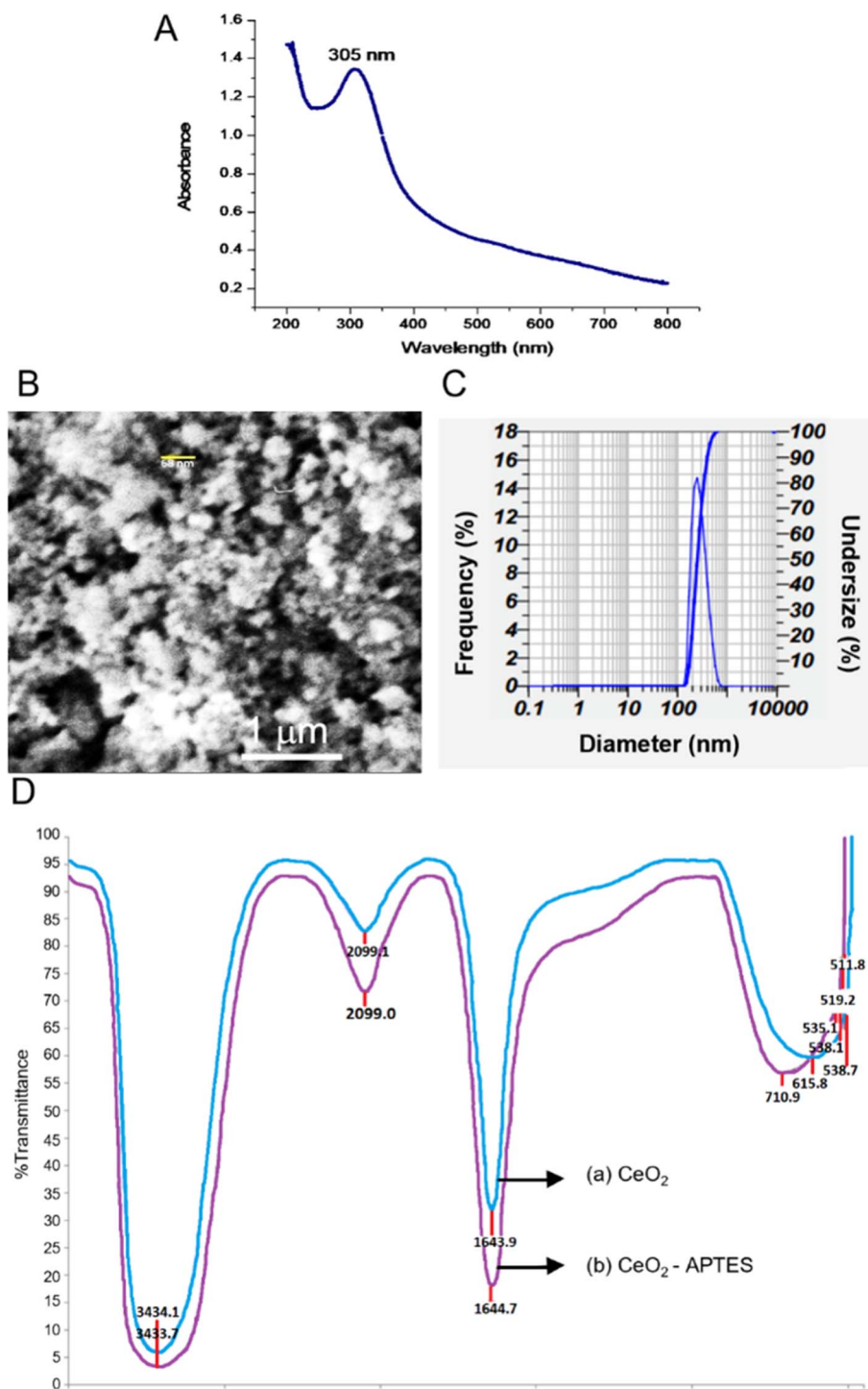


Fig. 2 (A) UV-Vis spectrum of CeO<sub>2</sub>; (B) SEM images of CeO<sub>2</sub> powder; (C) PSA spectrum of CeO<sub>2</sub>; (D) FT-IR Spectra of CeO<sub>2</sub> only (a), and those of APTMS-CeO<sub>2</sub> (b).

presence of CeO<sub>2</sub> on the surface of the SPCE which facilitates the charge transfer mechanism at the modified electrode interface. The decrease in current, 9.843 μA to 44.940%, was recorded on SPCE-CeO<sub>2</sub>@NH<sub>2</sub> after adding 2.5% GA (Fig. 4A(c)). The response decreases further 6.993 μA to 28.95% for SPCE-CeO<sub>2</sub>@NH<sub>2</sub>-GA-Aptamer (Fig. 4A(d)). The addition of GA and

aptamer to the electrode surface decreased the transferability of redox [Fe(CN)<sub>6</sub>]<sup>4-/3-</sup> electrons to the electrode, indicating that the aptamer had immobilized the electrodes. The SPCE-CeO<sub>2</sub>@NH<sub>2</sub>-Aptamer was treated with BSA, which acts as a blocking agent to cover non-specific species that can interfere with the analysis. In Fig. 4A(e), the addition of the Spike RBD



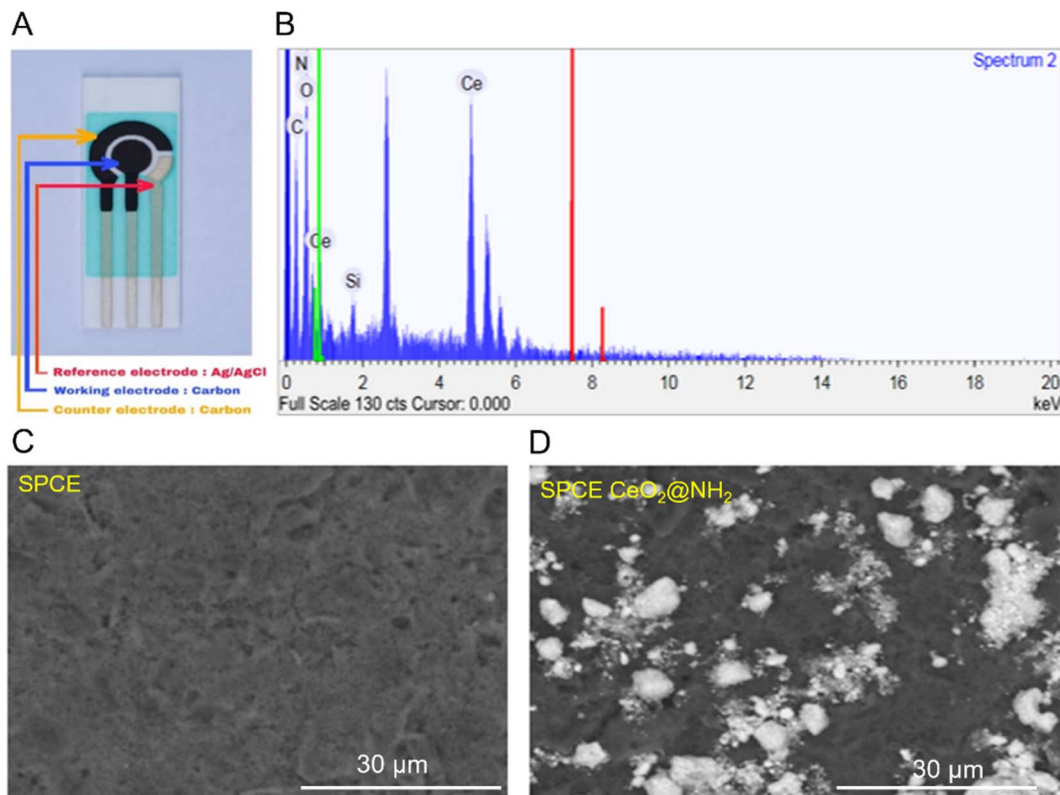


Fig. 3 (A) Screen-printed carbon electrode (SPCE); (B) EDS spectra of SPCE-CeO<sub>2</sub>@NH<sub>2</sub>; (C) SEM images SPCE bare; (D) SEM images SPCE-CeO<sub>2</sub>@NH<sub>2</sub>.

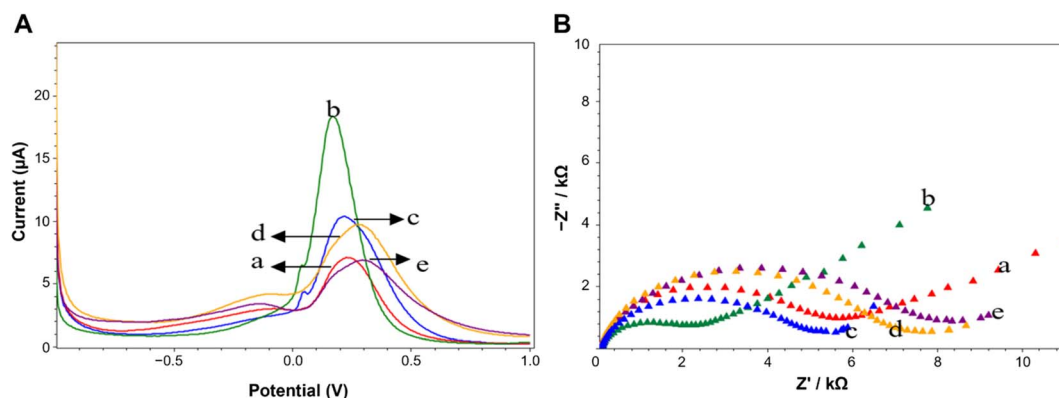


Fig. 4 (A) Differential Pulse Voltammogram (scan rate 0.008 V s<sup>-1</sup>, at potential range -0.1 V to +0.1 V) of (a) SPCE bare (b) SPCE-CeO<sub>2</sub>@NH<sub>2</sub> (c) SPCE-CeO<sub>2</sub>@NH<sub>2</sub>-GA (d) SPCE-CeO<sub>2</sub>@NH<sub>2</sub>-Aptamer (e) SPCE-CeO<sub>2</sub>@NH<sub>2</sub>-Aptamer-Spike RBD; (B) Nyquist plot (were recorded from 0.1 Hz to 100 kHz). Both using a redox system a redox of 10 mM K<sub>3</sub>[Fe(CN)<sub>6</sub>] with 0.1 M KCl in 0.05 PBS pH 7.4 on different.

results in a decrease in the current of 32.29% because the Spike RBD is a non-electroactive molecule obstructing the electron transfer process at the electrode. The increasing concentration of the Spike RBD is trapped on the electrode surface, decreasing the reduction current peak of [Fe(CN)<sub>6</sub>]<sup>4-/3-</sup>.

Additionally, Electrochemical Impedance Spectroscopy (EIS) is an important tool to study different aspects of interfacial behavior in surface-modified electrodes. EIS was performed to clarify the electrochemical response, as shown in Fig. 4B. The Nyquist plot

of each functionalization step affects the change in the size of the  $R_{ct}$ . GA incubation and immobilization of the aptamer at the electrodes increased the density of the coating on the electrodes, hindering the ability to transfer electrons (Fig. 4B(c) and B(d)). The increase in the diameter of the Nyquist plot occurs due to the aptamer-Spike RBD interaction. The spontaneous adsorption of the Spike RBD on the surface of the electrode hinders the ability of [Fe(CN)<sub>6</sub>]<sup>4-/3-</sup> electron transfer, thereby increasing the impedance and resistance, which are inversely proportional to



the measured height. Fig. 4B(a) and B(b) showed the EIS response for bare SPCE, and SPCE-CeO<sub>2</sub>@NH<sub>2</sub> respectively in the frequency of 1 mHz–100 kHz using 5 mM of [Fe(CN)<sub>6</sub>]<sup>4−/3−</sup> redox couple as the electrochemical probe. The Nyquist plot of EIS spectra consists of a semi-circular part in the high-frequency domain representing the charge transfer at a limited region and a linear part in the low-frequency domain representing the diffusion-controlled region. At high frequencies, the diameter of the semicircle gives the electron transfer resistance ( $R_{ct}$ ). The  $R_{ct}$  value of SPCE-CeO<sub>2</sub>@NH<sub>2</sub> was less than that of bare SPCE, thus revealing enhanced electron transfer kinetics between bare and CeO<sub>2</sub>@NH<sub>2</sub> modified SPCE, thus suggesting a very less resistance on the conduction pathway of the electron at the modified electrode and electrolyte solution interface. Furthermore, being rich in oxygen vacancies and hence ease of change of oxidation state of Ce in CeO<sub>2</sub>, could result in a better charge transfer mechanism<sup>52</sup> providing good electrochemical activity of the material.

### 3.3 Optimization of experimental conditions

The aptamer concentration ( $X_1$ ), immobilization time ( $X_2$ ), and Spike RBD incubation time ( $X_3$ ) were optimized using a Box–Behnken experimental design with the Minitab 18 program (Table 1). Each factor was designed with three different levels, namely the lowest level (−1), medium (0), and highest (+1), to obtain the following equation:

$$Y = 6.209 - 2.746X_1 - 0.947X_2 + 0.134X_3 - 0.039X_1^2 - 0.039X_2^2 + 2.175X_3^2 + 0.714X_1 \times X_2 - 0.249X_1 \times X_3 - 0.581X_2 \times X_3 \quad (1)$$

The value of the correlation coefficient ( $R^2$ ) of eqn (1) was 0.933, indicating a good fit.<sup>53</sup> From the regression equation above, a one-point increase in the aptamer concentration ( $X_1$ ) will decrease the current by 2.746%. The  $P$ -value and lack of fit (LOF) were 0.057 and 0.027, respectively. The LOF will be meaningless if the  $P$ -value in the variation model is smaller than  $\alpha = 0.05$ . Therefore, the resulting linear equation is acceptable. The optimal conditions from the Box–Behnken experimental design data were an aptamer concentration of 1.5  $\mu\text{g mL}^{-1}$ , aptamer

immobilization time of 60 minutes, and incubation of target Spike RBD for 10 minutes. The aptamer's optimal immobilization will affect the aptamer's stability on the electrode surface, thus allowing the formation of imide bonds between the aptamer and the maximum GA. Too high a concentration of aptamer allows steric hindrance at the electrodes, thereby interfering with the activity of the aptamer in recognizing the target. The mean probe-to-probe separation obtained at the highest density approximates the expected radius of this aptamer, which is believed to be partially folded in the absence of a target due to allowing it to pack less closely.<sup>54</sup> Also, the target incubation time is related to the duration of the test time; the longer the target incubation time, the more targets are tied to the aptamer.

### 3.4 Calibration curve

The calibration curve and LOD were calculated in the optimal experimental conditions. Spike RBDs with various concentrations of 0.001–100  $\text{ng mL}^{-1}$  were tested on the aptasensor and electrochemical response was measured using DPV in the [Fe(CN)<sub>6</sub>]<sup>4−/3−</sup> redox system containing 0.1 M KCl in PBS (0.1 M, pH 7.4). The detection principle is based on the change in peak oxidation current response ( $\Delta I$ ) before and after the aptamer target interaction. This peak current was evaluated using the following equation:  $\Delta I_{pa} = I_0 - I_n$ , where  $I_0$  is the current response before interaction, while  $I_n$  is the response after the aptasensor interacts with the target.

Fig. 5A shows the DPV current of various Spike RBD concentrations. The greater the Spike RBD concentration, the more Spike RBD species bound to the aptamer, hence the lower the measured peak current. The calibration curve consists of two linear curve segments in Fig. 5B with different slopes (two segments of the calibration curve are drawn separately). The calibration curve is linear over two concentration ranges from 0.001 to 1  $\text{ng mL}^{-1}$  and 0.1 to 100  $\text{ng mL}^{-1}$  (Fig. 5B). The corresponding calibration curve regression equations for lower and higher concentration ranges are  $\Delta I_{pa} = 9.6118 [\text{Spike RBD}] (\text{ng mL}^{-1}) + 1.554$  with  $R^2 = 0.9828$  and  $\Delta I_{pa} = 0.0179 [\text{RBD spike}] (\text{ng mL}^{-1}) + 2.5883$  with  $R^2 = 0.9914$ , respectively (Fig. 5). The LOD

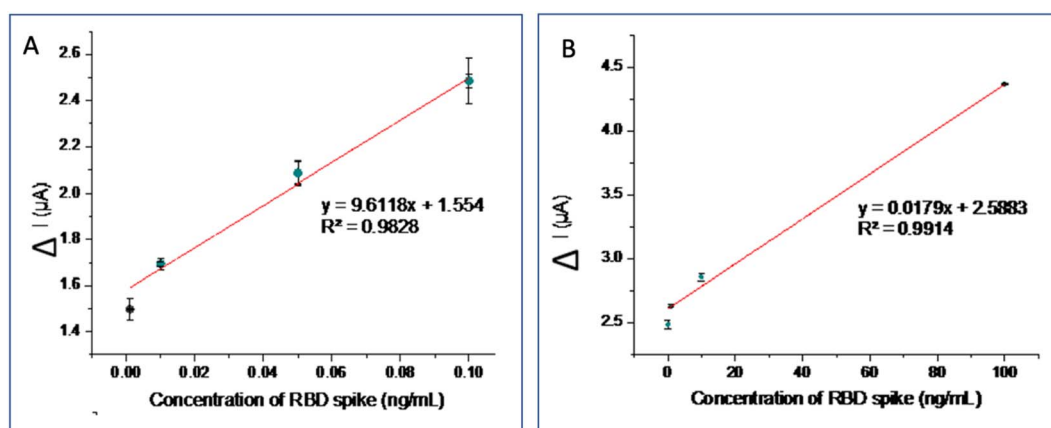


Fig. 5 (A) Curve calibration of RBD spike for concentration (0.001–1  $\text{ng mL}^{-1}$ ); and (B) those for concentration range (0.1–100  $\text{ng mL}^{-1}$ ) using redox system of 10 mM K<sub>3</sub>[Fe(CN)<sub>6</sub>] with 0.1 M KCl in 0.05 PBS pH 7.4.



Table 2 The data of precision and accuracy

Sample	$\Delta I$ ( $\mu\text{A}$ )	Average $\Delta I$ ( $\mu\text{A}$ )	SD	RSD (%)	Precision (%)	Accuracy (%)
Saliva	2.623 2.688 2.639 2.517 2.549 2.610	2.604	0.062	2.38	90.50	97.39

was  $0.017 \text{ ng mL}^{-1}$  and the LOQ was  $0.052 \text{ ng mL}^{-1}$ , with an accuracy of 90.50% and a precision of 97.38% (Table 2).

### 3.5 Selectivity of the aptasensor

The selectivity of a method is its ability to specifically measure certain analytes in the presence of other components that may be present in the sample matrix. The selectivity was determined for an inactive avian influenza virus (H5N1) which may present in the sample matrix and the measured current peak response was compared with the Spike RBD peak response. Fig. 6A shows the measured response of the H5N1 virus, which is  $4.281 \mu\text{A}$ , similar to the negative control (solvent without containing sample analyte) as PBS of  $4.269 \mu\text{A}$ , indicating that there is no binding between the aptamer and the H5N1 virus. Other treatments were studied to see the effect of interference in determining the percentage selectivity. Fig. 6B shows the measured peak response of  $2.444 \mu\text{A}$ , similar to the peak of the Spike RBD current response, namely  $2.312 \mu\text{A}$ , confirming that the aptamer is very good at recognizing the Spike RBD as a target. The existence of interference or interference does not affect the activity of the aptamer. The presence of H5N1 virus in the sample matrix showed a relative response of 94.29% aptamer. This shows the high selectivity of the Spike RBD aptamer to the target.

### 3.6 Evaluation of aptasensor performance using clinical samples

The performance of the electrochemical aptasensor was then evaluated using saliva samples and oropharyngeal swabs using

Table 3 Data of biological samples

Sample	$\Delta I$ ( $\mu\text{A}$ )	$\Delta I$ ( $\mu\text{A}$ )	SD	RSD (%)
Saliva	3.486 3.514 3.261	3.420	0.138	4.05
Oropharyngeal	3.414 3.449 3.492	3.451	0.038	1.11

Table 4 SARS-CoV-2 aptasensor data validation against nasopharyngeal swab samples and comparison with qRT-PCR

Sample of patient	RT-PCR	Aptasensor
1	(+)	(+)
2	(-)	(-)
3	(+)	(+)
4	(+)	(+)
5	(-)	(-)
6	(+)	(+)
7	(+)	(+)
8	(+)	(+)
9	(+)	(+)
10	(-)	(-)

a standard addition method. The salivary samples and oropharyngeal swabs from normal individuals were spiked with a  $50 \text{ ng mL}^{-1}$  Spike RBD. The percentage recovery were 92.96%, and 96.52% for the saliva samples oropharyngeal swabs respectively. This parameter is a measure of reproducibility of the sensor and it is seen that the RSD lies at 4.05% and 1.11%, respectively (Table 3), indicating that the developed aptasensor can be applied as a COVID-19 rapid test method for clinical samples.

The developed aptasensor was also has been tested on 10 samples from COVID-19 patients stored in PBS buffer. All samples were tested by the qRT-PCR method and showed a  $C_t$  value  $< 25$  and the results were shown in Table 4. However, based on the peak current obtained in clinical sample testing, which is between  $0.195\text{--}4496 \mu\text{A}$ , we suspect that samples with a  $C_t$  value  $> 25$  can still be detected.

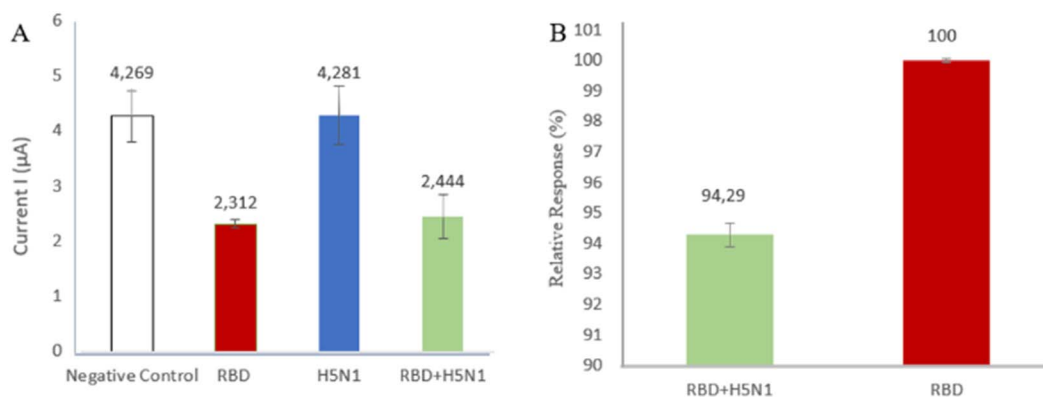


Fig. 6 (A) The comparison of current response H5N1 toward Spike RBD; (B) selectivity of aptamer toward Spike RBD.





Table 5 Comparison of performance of the developed biosensor electrochemical with the other existing types of SARS-CoV-2 spike detection

Method	Limit of detection	Linear range	Sample	Ref.
Electrochemical immunosensor based on graphene working a functionalized anti-spike	$20 \times 10^3$ ng mL <sup>-1</sup>	—	—	11
Electrochemical biosensor functionalized TiO <sub>2</sub> nanotube	0.7 nM	14–1400 nM	Nasal secretions, salivary	55
Electrochemical immunosensor based on magnetic beads modified carbon black printed electrode	19 ng mL <sup>-1</sup>	—	Salivary	12
Electrochemical sensor PET-gold electrode monoclonal antibody	—	—	Serum	13
Biosensor AuNP functionalized/nCoV-19Ab	—	—	—	9
Electrochemical aptamer based sensor using gold electrode	—	—	Salivary	27
Electrochemical aptamer based sensor using shrinky-dink electrode	1 ng mL <sup>-1</sup>	—	Salivary	28
Electrochemical aptasensor using SPCE-Cu <sub>2</sub> O for the spike RBD detection spike glycoprotein	$0.03 \pm 0.01 (\times 10^{-6})$ ng mL <sup>-1</sup>	$1 \times 10^{-5}$ to $1.2 \times 10^3$ ng mL <sup>-1</sup>	Salivary	56
Electrochemical impedance spectroscopy-based aptasensor using a carbon nanofiber-gold for the spike RBD detection	$7.0 \times 10^{-3}$ nM	$1 \times 10^{-2}$ to 64 nM	Salivary	57
Electrochemical aptasensor for SARS-CoV-2 antigen detection based on aptamer-binding induced multiple hairpin assembly signal amplification	$9.79 \times 10^{-6}$ ng mL <sup>-1</sup>	$50 \times 10^{-6}$ to 50 ng mL <sup>-1</sup>	—	58
Nanoscale electrode-aptamer-SARS-CoV-2 imaging by photo-induced force microscopy	$1.30 \times 10^{-3}$ nM (6.6 $\times 10^{-2}$ ng mL <sup>-1</sup> )	—	—	59
Folding-based electrochemical aptasensor	7 nM	—	—	29
Optimization electrochemical aptasensor using SPCE-Au	2.63 ng mL <sup>-1</sup>	—	Salivary	30
Electrochemical aptasensor using SPCE-CeO <sub>2</sub> functionalized aptamer for the RBD spike detection	$1.7 \times 10^{-2}$ ng mL <sup>-1</sup>	$1 \times 10^{-3}$ to $10^2$ ng mL <sup>-1</sup>	Salivary, oropharyngeal swab	This work

Table 5 compares the performance characteristics of electrochemical aptamer-based biosensors as a method of SARS-CoV-2 detection. Judging from the comparison of LOD data, the results of this work are greater than the results of other studies. However, the simpler work steps are the advantages of this method, and it can still be used for detection in clinical samples.

## 4 Conclusions

We have shown that the simple aptasensor can detect SARS-CoV-2 Spike RBD, which is indicated by changes in electrochemical signals resulting from the interaction between the Spike RBD and SPCE-CeO<sub>2</sub>@NH<sub>2</sub>-aptamer. These electrochemical aptasensor shows a fast (within 10 minutes) and accurate portable device with precision and accuracy of 90.50% and 97.39, respectively. Some of the materials used in electrochemical aptasensor have been reported, we show a comparison in Table 5. The electrochemical aptasensor is quite promising as a candidate for a SARS-CoV-2 diagnostic tool as an alternative to the qRT-PCR method.

## Ethical approval

The Research Ethics Committee Universitas Padjadjaran, has approved this study (registration no. 860/UN6.KEP/EC/2020). The study was conducted within the Biological Safety Cabinet Class II in the COVID-19 Laboratory (C-29 Lab), Universitas Padjadjaran.

## Author contributions

AT and HLW performed and conducted the experiments, drafted the manuscript; SNA, IA, AS, and DD analyzed the data; SG and MY supervised the study; YWH conceived the whole study. All authors were involved in manuscript editing.

## Conflicts of interest

There are no conflicts to declare.

## Acknowledgements

We thank Indonesian Ministry of Research, Technology and the National Innovation Agency for supporting this work with scheme No. 69/FI/P-KCOVID-19.2B3/IX/2020, and Universitas Padjadjaran Academic Leadership Grant No. 2203/UN6.3.1/PT.00/2022. The authors thank the School of Electrical Engineering and Informatics, Bandung Institute of Technology, for funding the article processing charge.

## References

- World Health Organization, <https://covid19.who.int/>, accessed 20 November 2022.



- 2 Y. Song, J. Song, X. Wei, M. Huang, M. Sun, L. Zhu, B. Lin, H. Shen, Z. Zhu and C. Yang, *Anal. Chem.*, 2020, **92**, 9895–9900.
- 3 S. Mavrikou, G. Moschopoulou, V. Tsekouras and S. Kintzios, *Sensors*, 2020, **20**, 1–12.
- 4 B. Diao, K. Wen, J. Chen, Y. Liu, Z. Yuan, C. Han, J. Chen, Y. Pan, L. Chen, Y. Dan, J. Wang, Y. Chen, G. Deng, H. Zhou and Y. Wu, *MedRxiv*, 2020, DOI: [10.1101/2020.03.07.200](https://doi.org/10.1101/2020.03.07.200).
- 5 G. N. Fadhilah, M. Yusuf, A. K. Sari, T. R. Tohari, H. L. Wiraswati, S. Ekawardhani, L. Faridah, N. Fauziah, I. Anshori and Y. W. Hartati, *ChemistrySelect*, 2023, **8**, e202203928.
- 6 P. D. Crook, J. R. Hospital and U. Kingdom, *ISARIC*, <https://isaric.tghn.org/>, accessed 20 November 2022.
- 7 S. Kang, M. Yang, Z. Hong, L. Zhang, Z. Huang, X. Chen, S. He, Z. Zhou, Z. Zhou, Q. Chen, Y. Yan, C. Zhang, H. Shan and S. Chen, *Acta Pharm. Sin. B*, 2020, **10**, 1228–1238.
- 8 Y. Li, L. Yao, J. Li, L. Chen, Y. Song, Z. Cai and C. Yang, *J. Med. Virol.*, 2020, **92**, 903–908.
- 9 A. Ahmadiwand, B. Gerislioglu, Z. Ramezani, A. Kaushik, P. Manickam and S. A. Ghoreishi, *Biosens. Bioelectron.*, 2021, **177**, 1–8.
- 10 T. Nguyen, D. D. Bang and A. Wolff, *Micromachines*, 2020, **11**, 1–7.
- 11 B. Mojsoska, S. Larsen, D. A. Olsen, J. S. Madsen, I. Brandslund and F. A. Alatraktchi, *Sensors*, 2021, **21**, 1–11.
- 12 L. Fabiani, M. Saroglia, G. Galatà, R. De Santis, S. Fillo, V. Luca, G. Faggioni, N. D'Amore, E. Regalbuto, P. Salvatori, G. Terova, D. Moscone, F. Lista and F. Arduini, *Biosens. Bioelectron.*, 2021, **171**, 112686.
- 13 M. Z. Rashed, J. A. Kopechek, M. C. Priddy, K. T. Hamorsky, K. E. Palmer, N. Mittal, J. Valdez, J. Flynn and S. J. Williams, *Biosens. Bioelectron.*, 2021, **171**, 1–6.
- 14 S. Mahari, A. Roberts, D. Shahdeo and S. Gandhi, *bioRxiv*, 2020, 1–20.
- 15 Z. Rahmati, M. Roushani, H. Hosseini and H. Choobin, *Microchim. Acta*, 2021, **188**, 1–9.
- 16 S. Kesavan, N. S. K. Gowthaman, S. Alwarappan and S. A. John, *Sens. Actuators, B*, 2019, **278**, 46–54.
- 17 Y. W. Hartati, D. Nurdjanah, S. Wyantuti, A. Anggraeni and S. Gaffar, *AIP Conf. Proc.*, 2018, **2049**(1), 020051.
- 18 S. Alwarappan, S. R. Singh, S. Pillai, A. Kumar and S. Mohapatra, *Anal. Lett.*, 2012, **45**, 746–753.
- 19 A. Sakthivel, A. Chandrasekaran, M. Sadasivam, P. Manickam and S. Alwarappan, *J. Electrochem. Soc.*, 2021, **168**, 017507.
- 20 A. K. Sari, S. Gaffar and Y. W. Hartati, *Anal. Bioanal. Electrochem.*, 2022, **14**, 127–143.
- 21 S. D. Jayasena, *Clin. Chem.*, 1999, **45**, 1628–1650.
- 22 B. Kayhan and U. Kayabas, *Dis. Mol. Med.*, 2013, **1**, 54–60.
- 23 S. M. Kim, J. Kim, S. Noh, H. Sohn and T. Lee, *Biochip J.*, 2020, **14**, 327–339.
- 24 L. Yang, L. Li, F. Li, H. Zheng, T. Li, X. Liu, J. Zhu, Y. Zhou and S. Alwarappan, *Anal. Bioanal. Chem.*, 2021, **413**, 193–203.
- 25 S. Zhang, H. Zheng, R. Jiang, J. Yuan, F. Li, T. Qin, A. Sakthivel, X. Liu and S. Alwarappan, *Sens. Actuators, B*, 2022, **351**, 130966.
- 26 Y. Tang, X. Liu, H. Zheng, L. Yang, L. Li, S. Zhang, Y. Zhou and S. Alwarappan, *Nanoscale*, 2019, **11**, 9115–9124.
- 27 A. Idili, C. Parolo, R. Alvarez-Diduk and A. Merkoçi, *ACS Sens.*, 2021, **6**, 3093–3101.
- 28 J. A. Zakashansky, A. H. Imamura, D. F. Salgado, H. C. Romero Mercieca, R. F. L. Aguas, A. M. Lao, J. Pariser, N. Arroyo-Currás and M. Khine, *Anal. Methods*, 2021, **13**, 874–883.
- 29 F. Curti, S. Fortunati, W. Knoll, M. Giannetto, R. Corradini, A. Bertucci and M. Careri, *ACS Appl. Mater. Interfaces*, 2022, **14**, 19204–19211.
- 30 A. K. Sari, Y. W. Hartati, S. Gaffar, I. Anshori, D. Hidayat and H. L. Wiraswati, *J. Electrochem. Sci. Eng.*, 2022, **12**, 219–235.
- 31 S. N. Zakiyyah, D. R. Eddy, M. L. Firdaus, T. Subroto and Y. W. Hartati, *J. Electrochem. Sci. Eng.*, 2022, 1–18.
- 32 R. C. de Carvalho, A. J. Betts and J. F. Cassidy, *Microchem. J.*, 2020, **158**, 1–11.
- 33 Y. W. Hartati, L. K. Letelay, S. Gaffar, S. Wyantuti and H. H. Bahti, *Sens. Bio-Sens. Res.*, 2020, **27**, 1–13.
- 34 M. Roushani and F. Shahdost-Fard, *Microchim. Acta*, 2018, **185**, 1–8.
- 35 J. T. Dahle and Y. Arai, *Int. J. Environ. Res. Public Health*, 2015, **12**, 1253–1278.
- 36 Y. W. Hartati, S. N. Topkaya, S. Gaffar, H. H. Bahti and A. E. Cetin, *RSC Adv.*, 2021, **11**, 16216–16235.
- 37 B. C. Nelson, M. E. Johnson, M. L. Walker, K. R. Riley and C. M. Sims, *Antioxidants*, 2016, **5**, 1–21.
- 38 M. Khairy, B. G. Mahmoud and C. E. Banks, *Sens. Actuators, B*, 2018, **259**, 142–154.
- 39 M. Muthukumar, C. Venkateswara Raju, C. Sumathi, G. Ravi, D. Solairaj, P. Rameshthangam, J. Wilson, S. Rajendran and S. Alwarappan, *New J. Chem.*, 2016, **40**, 2741–2748.
- 40 A. A. Azmi, A. H. Ruhaimi and M. A. A. Aziz, *Mater. Today Chem.*, 2020, **16**, 1–9.
- 41 Y. W. Hartati, D. R. Komala, D. Hendrati, S. Gaffar, A. Hardianto, Y. Sofiatin and H. H. Bahti, *R. Soc. Open Sci.*, 2021, **8**, 1–11.
- 42 M. Guler, V. Turkoglu, A. Kivrak and F. Karahan, *Mater. Sci. Eng., C*, 2018, **90**, 454–460.
- 43 S. Ismail, N. A. Yusof, J. Abdullah and S. F. Abd Rahman, *Materials*, 2020, **13**, 1–16.
- 44 D. Liu, C. Ju, C. Han, R. Shi, X. Chen, D. Duan, J. Yan and X. Yan, *Biosens. Bioelectron.*, 2021, **173**, 1–8.
- 45 I. Soussi, Z. Mazouz, P. Y. Collart-Dutilleul, M. Echabaane, M. Martin, T. Cloitre, R. M'ghaieth, F. J. G. Cuisinier, F. Cunin, C. Gergely and A. Othmane, *Colloids Surf., B*, 2019, **181**, 489–497.
- 46 Q. Wang, B. Zhang, X. Lin and W. Weng, *Sens. Actuators, B*, 2011, **156**, 599–605.
- 47 C. Carlomagno, D. Bertazioli, A. Gualerzi, S. Picciolini, P. I. Banfi, A. Lax, E. Messina, J. Navarro, L. Bianchi, A. Caronni, F. Marengo, S. Monteleone, C. Arienti and M. Bedoni, *Sci. Rep.*, 2021, **11**, 1–13.
- 48 K. Khiabani and M. H. Amirzade-Iranag, *Am. J. Infect. Control*, 2021, **49**, 1165–1176.



- 49 S. Tsunekawa, J. T. Wang, Y. Kawazoe and A. Kasuya, *J. Appl. Phys.*, 2003, **94**, 3654–3656.
- 50 M. M. Ali, H. S. Mahdi, A. Parveen and A. Azam, *AIP Conf. Proc.*, 2018, **1953**, 1–5.
- 51 A. Weibel, R. Bouchet, F. Boulc'h and P. Knauth, *Chem. Mater.*, 2005, **17**, 2378–2385.
- 52 P. Nayak, P. N. Santhosh and S. Ramaprabhu, *J. Nanosci. Nanotechnol.*, 2015, **15**, 4855–4862.
- 53 J. Hao, X. Fang, Y. Zhou, J. Wang, F. Guo, F. Li and X. Peng, *Int. J. Nanomed.*, 2011, **6**, 683–692.
- 54 R. J. White, N. Phares, A. A. Lubin, Y. Xiao and K. W. Plaxco, *Langmuir*, 2008, **24**, 10513–10518.
- 55 B. S. Vadlamani, T. Uppal, S. C. Verma and M. Misra, *Sensors*, 2020, **20**, 1–10.
- 56 Z. Rahmati, M. Roushani, H. Hosseini and H. Choobin, *Bioelectrochemistry*, 2022, **146**, 1–9.
- 57 M. A. Tabrizi and P. Acedo, *Biosensors*, 2022, **12**, 1–14.
- 58 J. Xue, Y. Li, J. Liu, Z. Zhang, R. Yu, Y. Huang, C. Li, A. Chen and J. Qiu, *Talanta*, 2022, **248**, 1–6.
- 59 J. C. Abrego-Martinez, M. Jafari, S. Chergui, C. Pavel, D. Che and M. Siaj, *Biosens. Bioelectron.*, 2022, **195**, 1–24.

